Wear 548–549 (2024) 205381

Contents lists available at ScienceDirect

Wear

journal homepage: www.elsevier.com/locate/wear

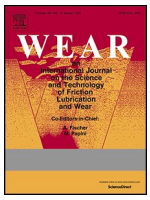

Tribology behaviour of graphene-modified nanostructured Al_2O_3/3 % TiO_2 coatings under boundary and mixed lubrication conditions

K.A. Habib [a,*], D.L. Cano [a], J. Serrano-Mira [a], Emilio Rayón [b], José V. Abellán-Nebot [a], S. Dosta [c]

[a] Department of Industrial System Engineering and Design, Universitat Jaume I, 12071, Castellón, Spain
[b] Institut de Tecnologia de Materials – Universitat Politècnica de València, Camino de Vera, s/n - 46022, Valencia, Spain
[c] SDT Group, Barcelona University, Gran Via de los Cortes Catalanes, 585, 08007, Barcelona, Spain

ARTICLE INFO

Keywords:
Oxygen-fuel
Nanostructured Al_2O_3/3 % TiO_2
Graphene nanoplatelet
Lubrication regime

ABSTRACT

This study is focused on the preparation of a self-lubricating coating via thermal spraying. This coating was designed to control friction and lubrication in both boundary lubrication (BL) and mixed lubrication (ML) regimes. We aimed to compare the tribological behaviour of nanostructured Al_2O_3/3 % TiO_2 and modified nanostructured Al_2O_3/3 % TiO_2 incorporating 3 % GNPs coatings deposited by Oxygen-Fuel (OF). The critical conditions for the transition from BL to ML were experimentally studied using a fundamental tribological concept known as the Stribeck curve. A lubricating film consisting of detached GNPs, Al_2O_3 nanoparticle debris, and a conventional lubricant effectively covers the surface material and improves the mechanochemical interactions between the surface material and lubricating oil, thereby enhancing the tribological performance. The introduction of GNPs is found to play an effective role in the lubrication regime, leading to an increase in microhardness, a decrease in the friction coefficient and wear volume of the Al_2O_3/3 % TiO_2 coating, and the steel counterpart disc. It noticeably improved the critical load-carrying capacity at different speeds during the transition from BL to ML regimes. The tribo-layer formed on the worn surfaces controls the tribological properties of the Al_2O_3/3 % TiO_2 + 3 % GNPs coatings.

1. Introduction

Nanostructured ceramic coatings have attracted increasing attention in modern industrial sectors such as machinery (moving mechanical assemblies), chemical engineering, and metallurgy because of their chemical inertness, resistance to wear, galvanic and high-temperature oxidation and corrosion, exceptional hardness, and strength, which extend the sustainability of mechanical design and manufacturing processes.

Among the various kinds of metal oxides, aluminum oxide (Al_2O_3) is the foremost broadly considered lattice for graphene-ceramic composites. Al_2O_3 has amazing properties including compression strength, hardness, wear resistance, thermal and electrical insulation, mechanical resistance and corrosion resistance indeed at tall temperatures [1,2]. In the recent years, enhanced mechanical properties in coating with nanoscale microstructure have been reported, leading to a growing interest in the study and analysis of this type of ceramic materials [3–6]. Nanostructured Al_2O_3/TiO_2 coatings have been developed to satisfy the requirements of extreme and demanding tribological applications [7–10]. Compared with conventional coatings, thermally sprayed nanostructured Al_2O_3/TiO_2 coatings have distinctive and superior properties, such as high hardness, good wear resistance, and excellent thermal shock resistance, owing to the held (remainder) nanostructure, particularly with partial melting of the nanostructured powders [11].

In order to improve the tribological properties, the microstructure, composition, hardness, and lubrication conditions are typically modified by doping or adding nanofibers, nanowhiskers and graphene platelets. Incorporating graphene into ceramic coatings results in excellent mechanical, thermal, and electrical conductivities. The chemical properties of graphene have attracted widespread interest in the field of tribology. Graphene is a two-dimensional nanolayered structure of ultrathin carbon atoms with mechanical properties that are superior to those of other carbon allotropes. Graphene exhibits high lubricity, considerably wear resistance and enhance the tribological properties of materials [12–16]. With the aggregation of graphene, wear was significantly reduced owing to the sliding wear properties of the coatings. Qin et al. [17] studied the preparation of Al_2O_3 coatings using a mixture of 0.2 wt% graphene and 0.2 wt% carbon nanotubes as the

* Corresponding author.
E-mail address: razzaq@esid.uji.es (K.A. Habib).

https://doi.org/10.1016/j.wear.2024.205381
Received 30 January 2024; Received in revised form 2 April 2024; Accepted 17 April 2024
Available online 24 April 2024

reinforcement. This strategy has been extensively employed to manufacture new materials based on graphene because it can improve the toughness and wear resistance of bulk ceramic coatings [1,18,19]. The inclusion of graphene in different proportions to ceramics such as ZrO_2, $CaSiO_3$, and Y_2O_3–Al_2O_3–SiO_2 improves the tribological properties of ceramic coatings and reduces the steady-state friction coefficient and wear volume [17,20,21]. Bian et al. [22] added graphene to chemically bonded phosphate ceramic coatings and investigated the role of graphene dispersion in enhancing wear resistance. Additionally, the graphene combined with alumina has attracted application such as a self-lubricant coating within kinematic joints which contributes to substantially enhance the tribology performance and longevity by forming a tribofilm layer [23,24].

These coatings are usually deposited employing the plasma sprayed (PS) technique, because the high temperature of this process is necessary to melt the ceramic feedstock powder particles, whereas a lower percentage of melt particles is often found when the high velocity oxygen-fuel (HVOF) process is used [25].

Oxygen-fuel (OF) process was used to deposit nanostructured Al_2O_3/TiO_2 and Al_2O_3/TiO_2 + 3 % graphene because it is easy to handle, economical, can deposit different material types (metallic, ceramic, and polymer), and is more adaptable to critical technologies used in various industries to deposit wear-resistant oxide coatings [26]. In the OF spray process, the mean particle temperature and velocity are approximately 300 m/s and 3200 °C, respectively.

In this study, we aimed to elucidate the effect of the addition of graphene-modified nanostructured Al_2O_3/3 % TiO_2 coatings under different lubrication conditions on the lubrication regimes and load-carrying capacity of frictional parts. Therefore, we used the Stribeck curve, which combines operational conditions such as applied load, velocity, and fluid viscosity as a function of the friction coefficient. The friction regimes for sliding lubricated surfaces are broadly classified into (I) solid/boundary lubrication (BL), (II) mixed (ML), and (III) hydrodynamic (HL) [27].

Accordingly, we attempted to develop a thermal-spray graphene-modified nanostructured ceramic coating, which was deposited using the OF technique. The objective of this study was to investigate the potential application of graphene platelet-modified nanostructured Al_2O_3/3 % TiO_2 coatings under optimised working conditions to ultimately develop a thermally sprayed nanostructured ceramic coating with excellent mechanical and tribological properties. We particularly focused on the friction reduction mechanisms, lubrication regime parameters, and load-carrying capacity using the Stribeck curve. Initially, we prepared a feedstock powder by incorporating 3 % graphene into the nanostructured Al_2O_3/3 % TiO_2 coatings. Subsequently, the microstructures, porosities, and tribological properties of the coatings were evaluated. The wear scar depth and surface roughness of the modified coating were considerably lower than those of the unmodified Al_2O_3/TiO_2 coating. This experimental investigation provides a theoretical reference for the development and application of graphene in ceramic coatings such as nanostructured Al_2O_3/3 % TiO_2 to improve the tribological properties and microstructures of thermally sprayed ceramic coatings. The incorporation of graphene is considered to enhance the ability of the oil lubricant to produce continuous oil surface layers, resulting in a lower friction coefficient, higher load-carrying capacity, and improved critical conditions (higher load and lower speed) for the transition from BL to ML.

2. Experimental

2.1. Materials and feedstock powder

Stainless steel 304 was selected as the base metal because of its excellent mechanical properties and resistance to high-temperature oxidation. The test samples consisted of a rod with a diameter of 8 mm and length of 18 mm. The chemical composition (in wt%) of the base metal substrate was 17.5–19.5 % Cr, 8–10 % Ni, 2 % Mn, 1 % Si, 0.11 % N, 0.07 % C, 0.05 % P, and 0.03 % S; the rest was Fe. Two types of feedstock powder were deposited onto one end of the AISI 304 pins. The first type was Rototec 51,000, a commercial powder supplied by Castolin Eutectic, with 88.1 % Ni, 6.04 % Al, 5.25 % Mo, 0.36 % Fe and 0.22 % Cr by weight and a grain size of 40–13 μm; this powder served as a coupling layer between the base metal substrate and ceramic top layer. The second type of powder used in these experiments included a nanostructured ceramic (Al_2O_3/3 % TiO_2) finishing layer, referenced as Nanox S2603S, and modified nanostructured Al_2O_3/3 % TiO_2 reinforced with 3 % graphene feedstocks. These ceramic powders were purchased from Inframat Advanced Materials (USA). The initial powder nanoparticles with an average size ranging from 30 to 60 nm were prepared in suspension. These were then spray-dried, resulting in granules with a particle size distribution between 5 and 30 μm and a spherical morphology.

Graphene composed of 2–6 layers of carbon atoms arranged in hexagons in a honeycomb structure, with Brunauer–Emmett–Teller area >250 m^2/g, >98 % purity, average particle size of 10–30 μm and a flack thickness of 0.8–2 nm was used in this study. The scanning electron microscopy (SEM) images in Fig. 1a and b depict the nanoparticle morphology of the ceramic top coating layers of nanostructured Al_2O_3/3 % TiO_2 and modified Al_2O_3/3 % TiO_2 + 3 % graphene. Graphene was dispersed in the nanoparticles of the Al_2O_3/3 % TiO_2 feedstock powder (Fig. 1c). Magnified details of the graphene morphology and energy-dispersive X-ray (EDX) microanalysis are depicted in Fig. 1d and e, respectively. The graphene and nanostructured Al_2O_3/3 % TiO_2 powders were mixed uniformly, and the particle size was in accordance with the requirements for OF spraying.

To control the uniformity of the powder mixture and ensure homogeneity, the modified feedstock powder mixtures (3 wt% graphene and 97 wt% nanostructured Al_2O_3/3 % TiO_2 powders) were prepared using a Turbula rotative mixer for 5 h at 300 rpm. A HORIBA Jobin.

2.2. Thermal spraying procedure

The flame spraying of the bonding layers and nanostructured ceramic samples Al_2O_3/3 % TiO_2 and Al_2O_3/3 % TiO_2 + 3 % graphene was performed using an OF torch with a neutral oxyacetylene flame (CDS-8000, Castolin Eutectic). The parameters of the thermal deposition process for both coatings are listed in Table 1. Before the thermal spraying operation in order to eliminate grease and oxide surface contamination, and to improve the adherence between the coating and the substrate, the surfaces of the specimens were degreased with acetone and alcohol and grit-blasted with corundum particles (99.6 % purity and 36-mesh grit size) for 1 min at 0.2 m and an incident angle of approximately 45°, under an air pressure of 6 kg/cm^2. The objective of this step was to obtain a surface with a mean roughness of approximately $R_a \approx 6.1 \pm 0.5$ μm as measured using an optical surface profiler (Sensofar PLu 2300). This activation (roughening) operation enabled mechanical bonding (adhesion) between the coupling layer and the base metal substrate.

2.3. Microstructure

The coated samples were cut using a precision diamond blade saw and cold-mounted onto a polyester resin. Subsequently, the ceramic finish layer surface (Al_2O_3/3 % wt% TiO_2 and Al_2O_3/3 % wt% TiO_2 + 3 (wt% GNPs) cross sections were ground and polished using standard metallographic techniques. The diamond slurry polishing was performed in three sequential steps, using grain sizes of 6, 3, and 1 μm; finally, the specimens were lapped with Al_2O_3 paste and ultrasonically cleaned with acetone for 15 min.

Cross-sectional metallographic samples were prepared to quantitatively evaluate the porosity of the produced deposits. Optical microscopy images of the cross sections were studied. The coated specimens

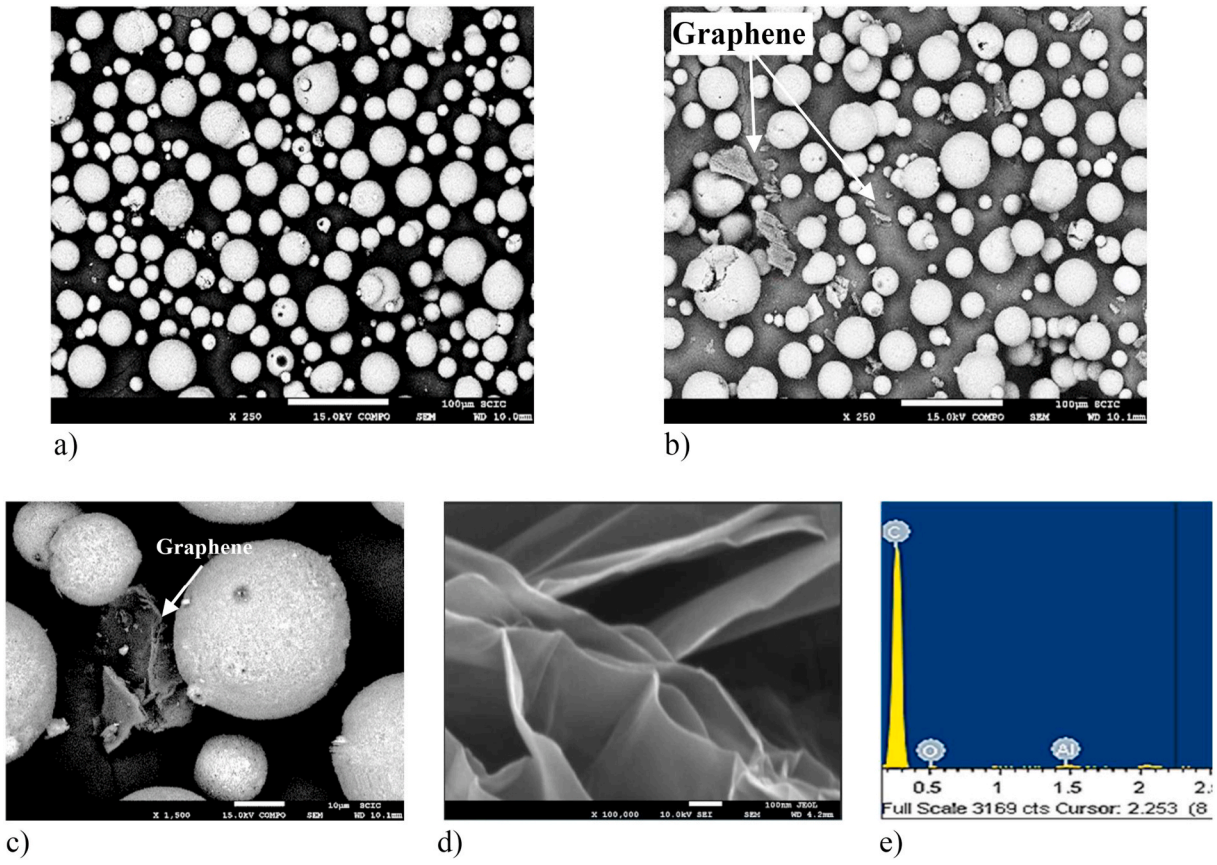

Fig. 1. a) SEM images of both types of ceramic feedstock powder: a) unmodified nanostructured Al_2O_3/3 % TiO_2 and b) modified nanostructured Al_2O_3/3 % TiO_2 + 3 % GNPs; c) details of GNPs distribution, d) magnified view of graphene morphology, and e) EDX microanalysis of graphene.

Table 1
Thermal spray parameters.

Torch velocity (m/s)	Sprayed alloy	Preheating stroke Nº	Spray stroke Nº	Spraying distance (mm)	Compressed air pressure (bar)
67.5	Rototec 51,000	1	1	150	1.5
67.5	97/3	0	6	85	3

were sectioned perpendicular to the ceramic top coating surface using the diamond cutting disc technique. The samples were prepared according to ASTM E1920. The microstructures of the ceramic-deposited coatings, in terms of polished surfaces and cross sections, were analysed using optical microscopy, SEM (JOEL 7001 F EDX-WDX Oxford) and energy dispersive spectroscopy (EDX) on the cross-section of a sample hot-mounted in epoxy resin. The phase identification of the feedstock powder and deposited coatings was conducted using a Siemens D5000 type X-ray diffractometer (XRD) with monochromatic nickel filtered Cu-Kα radiation at 20 mA and 35 kV. The scanning speed and goniometer range were chosen 2°/min and 2–70°, respectively. For the deposited coatings, the volume fractions of each phase were calculated using the Pearson VII function in the Origin software (OriginLab Company, Northampton, MA, USA) according to the integrated areas of each phase on the corresponding XRD patterns. The equation used is as follows:

$$V_{f,i} = \frac{A_i}{\sum A_i} \quad (1)$$

HORIBA Jobin Yvon Raman spectrometer configured at 514.5 nm emission was used to characterize some coated sample cross-sections. The localization of the analysis spot of the argon-ion laser was driven by an optical microscope (Nikon LV-100) under dark field illumination.

2.4. Microhardness and tribology characteristics

Vickers microhardness indentation measurements were performed along the cross section of the nanostructured ceramic Al_2O_3/3 % TiO_2 and Al_2O_3/3 % TiO_2 + 3 % graphene platelet coatings using an HMV Shimadzu Microhardness tester according to ISO 6507. The microhardness profile across the cross section of the nanostructured ceramic coatings was obtained in accordance with the standard test method ASTM E384 by applying a 100 g load for 15 s. Six measurements were performed at each distance, and the average values were computed in this study. The counterpart disc sample composed of quenched and tempered F-5220 steel (average hardness = 930 H V, mean surface roughness = 0.25 μm and density of 7850 kg/m^3) was used to perform the tribological tests.

The tribological performance of the top-deposited nanostructured ceramic coatings was evaluated using a TE79/P pin-on-disc multi-axis tribometer (Plint and Partners) for unidirectional sliding under laboratory conditions. Ten drops per minute of the mineral oil, CUT-MAX 110 (viscosity = 100 ± 0.1 cSt at 40 °C and density = 0.880 g/cm^3 at 15 °C), were applied to the contact area. The friction coefficients and tribological test parameters are listed in Table 2.

The wear test parameters are summarized in Table 2. The tests were interrupted at each 60 m test run in order to determine the variation in mass loss over a total sliding distance of 180 m. The wear loss of the pins or disc was determined gravimetrically by using a microbalance, and ultrasonic cleaning was carried out for each of them (pins and disc). The weight variation of the specimens after the test completion was measured as a decrease in the weight of pins and disc in grams. Volume

Table 2
Friction coefficients and tribological test parameters.

Parameters	Values Friction and wear test	Stribeck curve test
Load (N)	20	3, 6, 9, 12, 15, 18 and 21
Slip radius (mm)	35	35
Sliding velocity (m/s)	0.07	0.04, 0.07, 0.11, 0.14, 0.18 and 0.21
Sliding time (s)	3800	660
Distance (m)	271	600
Temperature (°C)	20	20
Relative humidity (%)	52	52

loss (mm^3) of the samples was calculated by dividing weight loss by density of the coating. The coating density was calculated using Archimedes principle, (in accordance with the ISO 21714:2018). The density of unmodified and modified coatings was found to be 1990 kg/m^3 and 2480 kg/m^3, respectively.

Wear rates were calculated using the mean measurement value of ceramic coatings and steel disc in terms of the volume of the coating material removed per unit load and sliding distance, in unit of $mm^3 \cdot N^{-1} m^{-1}$. At least three wear tests were performed for each type of ceramic coating and their results were reproducible within 5 %.

3. Results and discussion

3.1. Cross-sectional observation

Cross-sectional SEM images of the OF-sprayed nanostructured Al_2O_3/3 % TiO_2 coating and that modified with 3 % graphene are shown in Fig. 2a and b respectively. The effective bonding with the substrate and the absence of delamination indicate that the processing parameters selected in this study facilitated the deposition of high-quality coatings via the OF technique. As can be seen, both ceramic coatings exceeded 510 μm in thickness and a typical mechanical bonded form between the ceramic coating/bonding layer/substrate base metal, and the interface is quite uneven. The deposited coatings exhibited typical microstructures that are commonly observed in thermal spray coatings.

Typical defects of OF-deposited coatings (pores and microcracks) were observed in the studied coatings. The unmodified Al_2O_3/3 % TiO_2 coating had inherent pores, voids, and cracks (Fig. 3a). Pores and vertical cracks were easily observed. Vertical microcracks emerged in the coatings because of the deformation mismatch between the cold splats deposited in the initial stages during the build-up of the coating and the hot splats deposited in the subsequent stages [28]. The main cause of defects in OF-sprayed ceramic coatings has been identified as residual thermal stress, resulting in cracks and relatively low-impact kinetic energy of unmolten or semi-molten particles, which are responsible for the appearance of pores [29]. A cross-sectional view of the modified Al_2O_3/3 % TiO_2 coating (Fig. 3b) reveals that the initial pores were filled with a substantial amount of the powder material. The enlarged image in Fig. 3d indicates that the morphology of the composite powders deposited inside the PM zones (partially melted) is similar to that of the feedstock powders generated outside the coating under the same conditions. These zones are surrounded by a fully melted (FM) matrix.

Fig. 3c and e presents the qualitative chemical microanalysis based on EDX patterns for various zones in the unmodified nanostructured Al_2O_3/3 % TiO_2 and modified coatings, respectively. The areas dominated by (G, H, and I) confirm the presence of graphene (wt%) in the modified coating (Fig. 3e and f).

3.2. Porosity evaluation

The formation and development of porosity during the thermal spraying of coatings is primarily attributed to improper fusion between the spray feedstock particles or the generation of gaseous expansion. As all spray parameters were steadily maintained for both ceramic coatings, the determination of the porosity and its distribution was crucial to observe the effect of graphene aggregation and the suitability of the coating for its intended purpose. Both samples were cold mounted in epoxy, roughened and polished (see section 2.3). SEM images were used for microstructural observation and porosity evaluation. The cross sections of the coatings were analysed using Image-Pro Plus software to calculate the porosities of both coatings. The coating porosity was measured based on the optical images obtained from different locations (Fig. 4a–and b). The reported values indicate the average porosities. The measured porosity of the unmodified ceramic coating was approximately 25.1 %; after adding graphene, the porosity of the coating decreased to approximately 6.6 %.

The porosity of OF-deposited coatings is strongly related to the spreading behaviour of molten droplets of Al_2O_3/3 % TiO_2. Thermally sprayed coatings are formed by the deposition of completely melted and/or semi-melted droplets. Most of the pores on the surface of the (ceramic) coating consist of unmelted particles, primarily because the alumina (Al_2O_3/3 % TiO_2) particles approach the nanometre size (feedstock powder size). Moreover, the porosity of the agglomerated powder limits the heat transfer to the centre during the heating and flight of the droplet, resulting in external melting and some unmelted alumina powder inside the agglomerated powder. When the droplet strikes the substrate, the unmelted alumina powder bounces and adheres

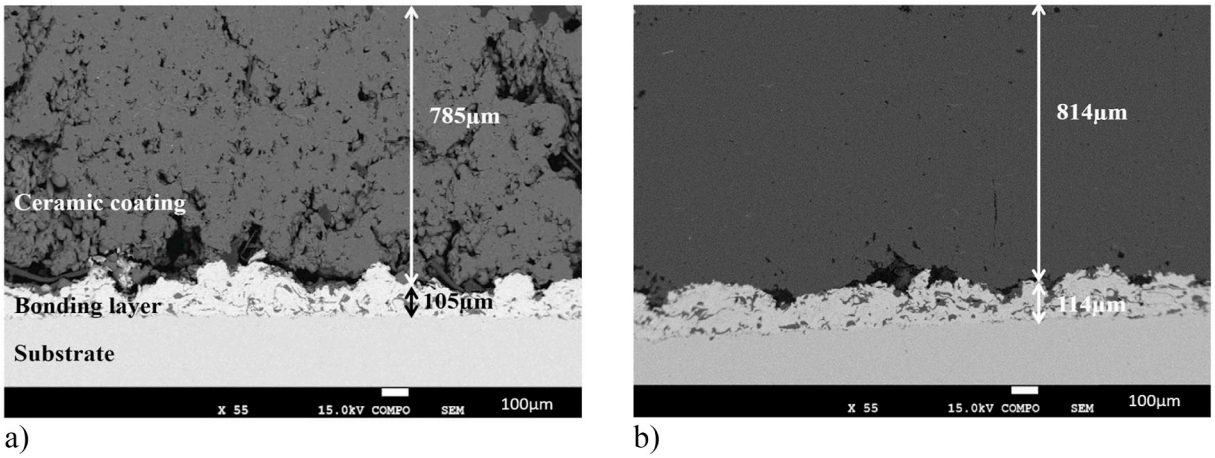

Fig. 2. Typical SEM cross-sectional micrographs of cross section showing the thickness of coatings deposited via the OF technique; a) Al_2O_3/3 % TiO_2 and b) Al_2O_3/3 % TiO_2 + 3 % graphene.

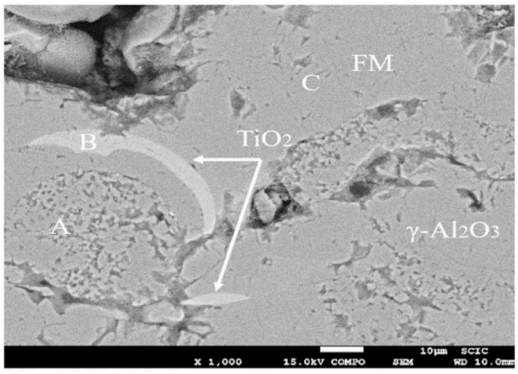

a) Al_2O_3 /3%TiO_2

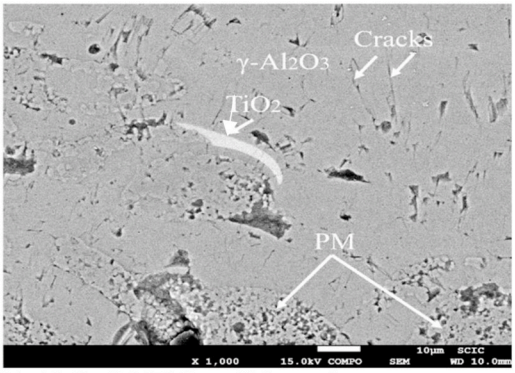

b) Al_2O_3 /3%TiO_2 + 3% graphene

Points	O wt %	Al	Ti
A	58.19	40.53	1.27
B	57.33	26.05	16.62
C	61.20	37.56	1.24
D	59.01	25.55	15.43
E	61.25	37.81	0.94

c)

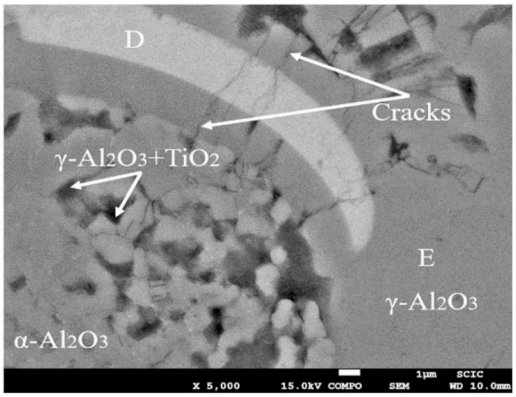

d) Al_2O_3 /3%TiO_2 + 3% graphene

Points	O wt %	Al	Ti	C
F	62.25	37.75	(**)	(**)
G	47.70	25.73	(**)	26.56
H	45.45	25.36	(**)	29.20
I	40.93	25,37	(**)	33.71

e)

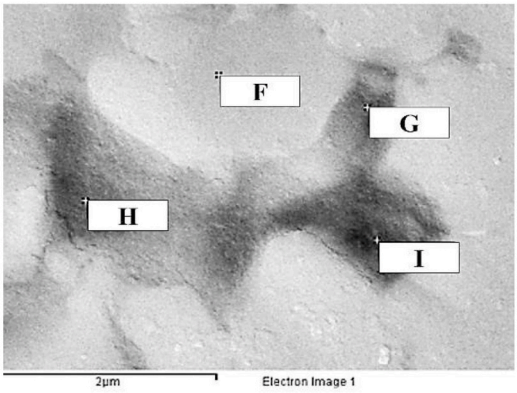

f)

Fig. 3. SEM cross-sectional microstructure of Al_2O_3/3 % TiO_2 coatings deposited by OF: a) unmodified and b) modified with 3 % graphene platelets; c) EDX elemental distribution of different zones; d) high-magnification image of the modified coating; e) EDX of graphene; f) detail of graphene localization.

to the lamellar surface. The unmelted ceramic particles markedly affect the deposition of the subsequent droplets, resulting in coatings with higher porosity. Combined with the low thermal conductivity of alumina, the gaps in the collision area are partially filled by the outwardly diffusing liquid, thus forming pores. Additionally, the incorporation of graphene with high thermal conductivity (5000 W/m K) and specific surface area to ceramic coatings with low thermal conductivity (36 W/m K) provides additional surface-active sites to improve the bonding strength between graphene and the other materials [30]. Owing to its exceptionally high thermal conductivity and heat dissipation, graphene facilitates the movement of gases in the nanostructured ceramic (Al_2O_3/3 % TiO_2 + 3 % graphene) coating during thermal deposition and reduces the porosity [31].

Furthermore, the effect of GNPs addition on the value of surface parameters (Rk, Rpk, Rvk, Mr1, Mr2) of both coatings was studied. The functional parameters were determined using Abbott-Firestone curve. The three functional parameters, Rpk (the first region of contact), R_k (the working region of contact or the core height) and Rvk (the lubricant retention region or the valley depth), selected for evaluating the topography of unmodified and modified coatings are presented in Fig. 5a and b, respectively, as they are extracted from the coatings curve for a 2D profile. The using of Abbott-Firestone curve is considered necessary method to represent the distribution of the height of peaks and valleys in the roughness profile, and it is important to introduce specific characteristics related to surface integrity and functional requirements for certain application.

The highest values of Rpk and Rk were obtained with the unmodified (with higher porosity contain) coating. The Rpk parameter decreased

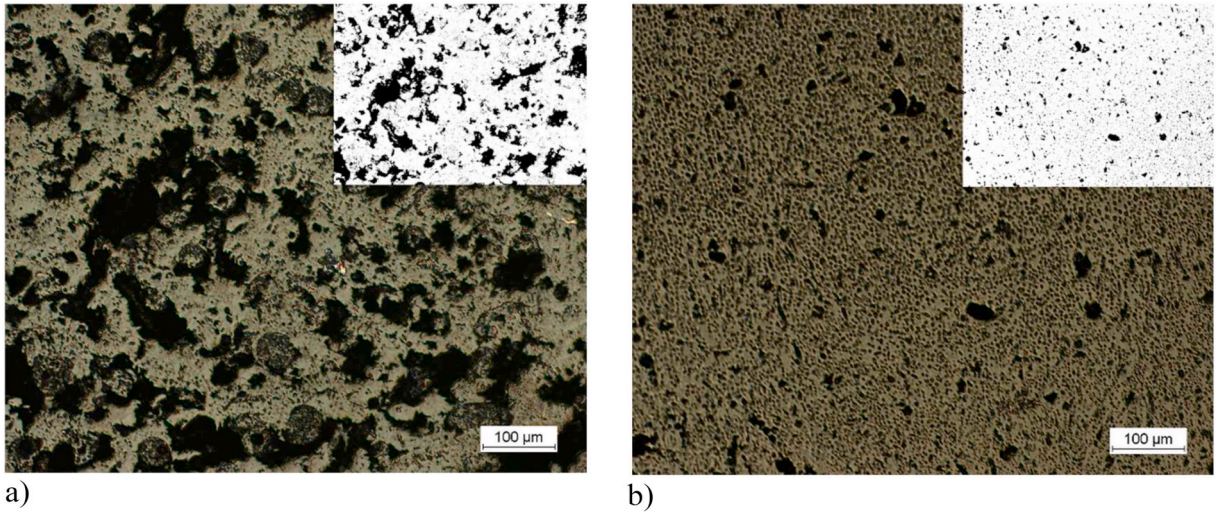

Fig. 4. Optical microscopy images of the cross sections of the deposited coatings; a) nanostructured Al_2O_3/3 % TiO_2 and b) Al_2O_3/3 % TiO_2 + 3 % graphene coatings.

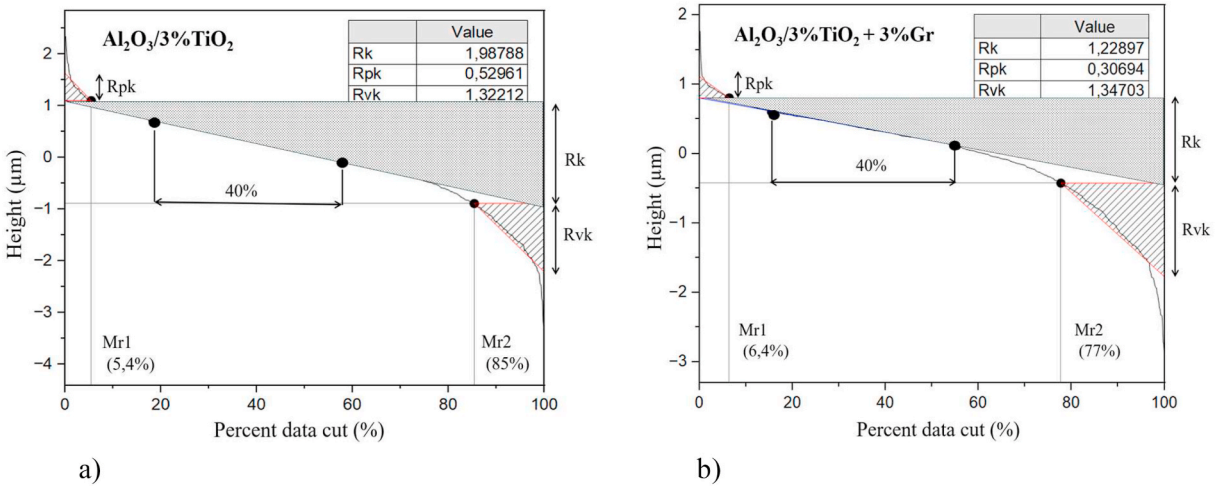

Fig. 5. Abbott-Firestone curves, the set of functional parameters R_{pk}, R_k and R_{vk} of; a) unmodified nanostructured Al_2O_3/3 % TiO_2 and b) modified coating nanostructured Al_2O_3/3 % TiO_2+3 % GNPs.

with the modified coating from 0.52 to 0.3 and the R_k from 1.98 to 1.22. Relatively similar values of the Rvk (1.32 and 1.34 for unmodified and modified coatings respectively) parameters are obtained with both coatings. This can be explained by the fact that the profiles of both surface coatings are characterized by the similar sharp depressions, which is probably favorable for the obtained dependencies. While, Mr1 and (100-Mr2) represent the portions of the surface covered by peaks and valleys, respectively, and define the two black regions. Rpk and Rvk represent the height of the triangles having the same area of those regions. In tribology, Mr2 represents the load-bearing surface.

3.3. X-ray diffraction analysis

The main crystalline phases that occurred during the change from the spray feedstock powder to the deposited state were analysed using the X-ray diffraction (XRD) patterns of nanostructured Al_2O_3/3 % TiO_2 and Al_2O_3/3 % TiO_2 + 3 % graphene. As shown in Fig. 6a and b, the XRD results of the initial nanostructured powder Al_2O_3/3 % TiO_2 and as-sprayed coatings were in good agreement with previously reported findings, as the typical peaks predominantly consisted of stable rhombohedral (a = 4.759; c = 12.991 Å) α-Al_2O_3. The rutile phase of TiO_2 and metastable Al_2TiO_5 phase with a pseudobrookite structure were observed in the nanostructured powder and deposited coating. The low intensity of the TiO_2 peak is probably because most of the Ti ions dissolved in the Al_2O_3 crystal lattice or defects [32]. However, Al_2TiO_5 in the initial powder is considered to have formed during crushing and fusing. The partial transformation of α-Al_2O_3 to cubic γ-Al_2O_3 (a = 7.9 Å) and tetragonal or orthorhombic δ-Al_2O_3 in the deposited coating can be attributed to the thermal spraying parameters and heat conditions during cooling process. Vreeling et al. [33] reported that a cooling rate of 400 K/s (400 °C/s) is sufficiently high to form the metastable γ-Al_2O_3 phase. Moreover, the amount of γ-Al_2O_3 is primarily determined by the actual cooling rate between 1200 K (926.85 °C) and 800 K (526.85 °C), wherein γ-Al_2O_3 is formed. Because of rapid cooling, the atoms cannot be arranged to form stable α-Al_2O_3; consequently, the disordered γ-Al_2O_3 phase is formed. Above approximately 1200 K (926.85 °C) α-Al_2O_3 is formed [33]. At temperatures exceeding 800 K (526.85 °C), γ-Al_2O_3 is topotactically transformed into tetragonal δ-Al_2O_3 [34,35]. Generally, δ-Al_2O_3 is considered to require less thermal activation and is the preferred type of phase to form at the lower range of high-temperature treatment [36]. The XRD patterns of the 3 % graphene feedstock and coatings are shown in Fig. 6b. A peak attributed to graphene was detected in the powder and the modified deposited coating. The diffraction peak intensity and width of the graphene were higher in

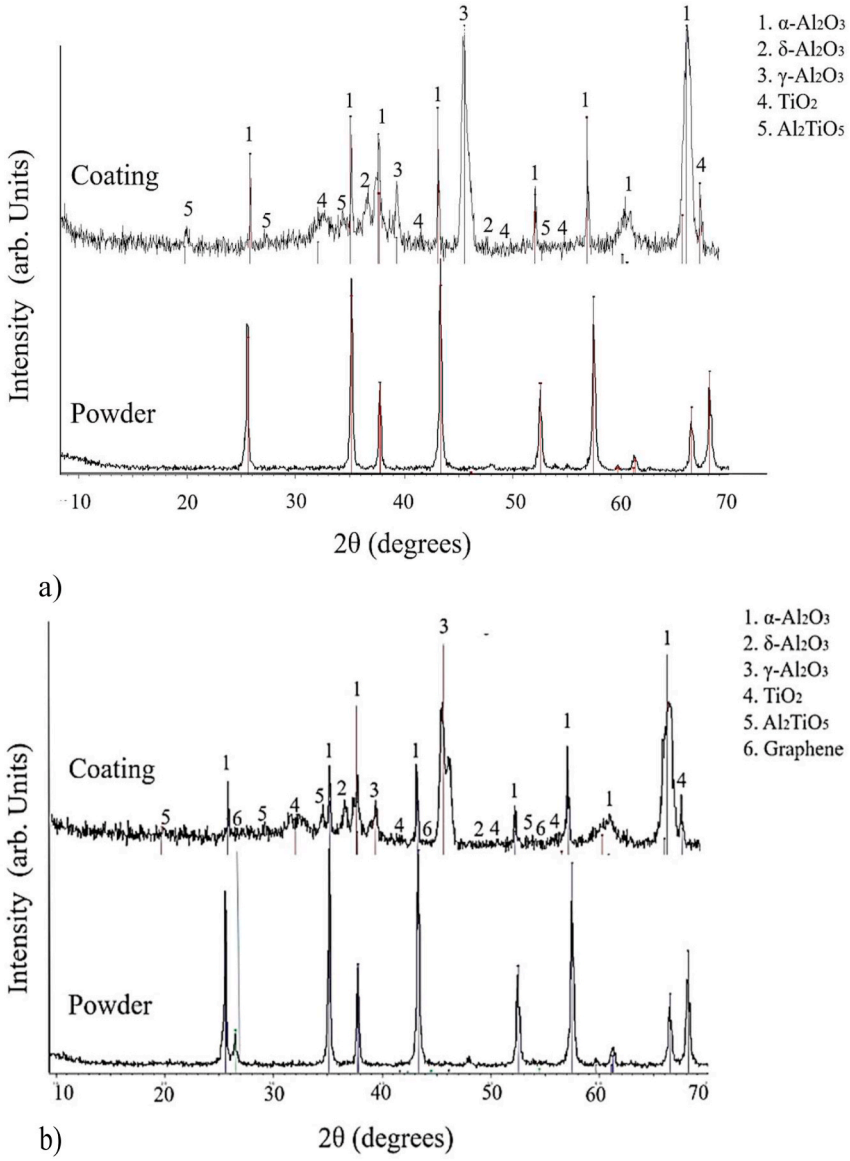

Fig. 6. XRD patterns of nanostructured Al_2O_3/3 % TiO_2: a) unmodified and b) modified with 3 % graphene, feedstock spraying powder, and deposited coatings.

the powder than in the deposited coating. Compared to the unmodified and modified powders and coatings, no appreciable phase modifications were detected after the addition of graphene.

Based on the XRD pattern of the deposited coatings, the volume fractions of the phases were calculated considering the integrated peak areas of each phase on the corresponding XRD patterns [37,38]. Practically no changes were observed in the volume fractions of the different phases in both ceramic coatings (Table 3). Additionally, the ratio of the three Al_2O_3 phases in the coating is due to the heat conditions during the cooling process of the deposited coating [39–42].

The weak intensity peak of graphene in the XRD pattern indicates that product purity nature and less amount of graphene was incorporated in the Al_2O_3 crystal framework. Fig. 7a and b, show the graphene platelet dispersed in the Al_2O_3 coating matrix. Fig. 7c, shows the observed Raman spectra for the modified coating. Spectra for graphene exhibit sharp peaks at the wave numbers of 1350, 1554 and 2750 cm^{-1} representing D, G, and 2D bands respectively.

Table 3
Volume fraction (vol%) of each phase of the deposited coatings calculated using integral areas from the XRD patterns.

Coating	α-Al_2O_3	δ-Al_2O_3	γ-Al_2O_3	TiO_2	Al_2TO_5	Graphene
Al_2O_3/3%TiO_2	62.9	3.2	25.1	5.9	3.0	0.0
Al_2O_3/3%TiO_2 + 3%Gr	60.1	2.4	27.6	7.5	2.0	0.3

3.4. Microhardness investigation

The evolution of the microhardness profile of the ceramic coating surface towards the bonding layer and base metal substrate for both the unmodified nanostructured Al_2O_3/3 % TiO_2 coating and that modified with 3 % graphene is shown in Fig. 8a. Microhardness measurements were performed five times at each point. Features such as porosities and their orientation and the unmelted and/or semi-molten content were found to affect the microhardness of the deposited coatings produced via thermal spraying [43]. The difference between the hardness of the coatings and that of the substrate was evident. The fluctuation in the microhardness along the cross section is associated with structural changes in the cross section of the coatings [44]. After adding 3 % graphene to the nanostructured Al_2O_3/3 % TiO_2, the microhardness of the coatings was approximately 1471 ± 52 H V, which was

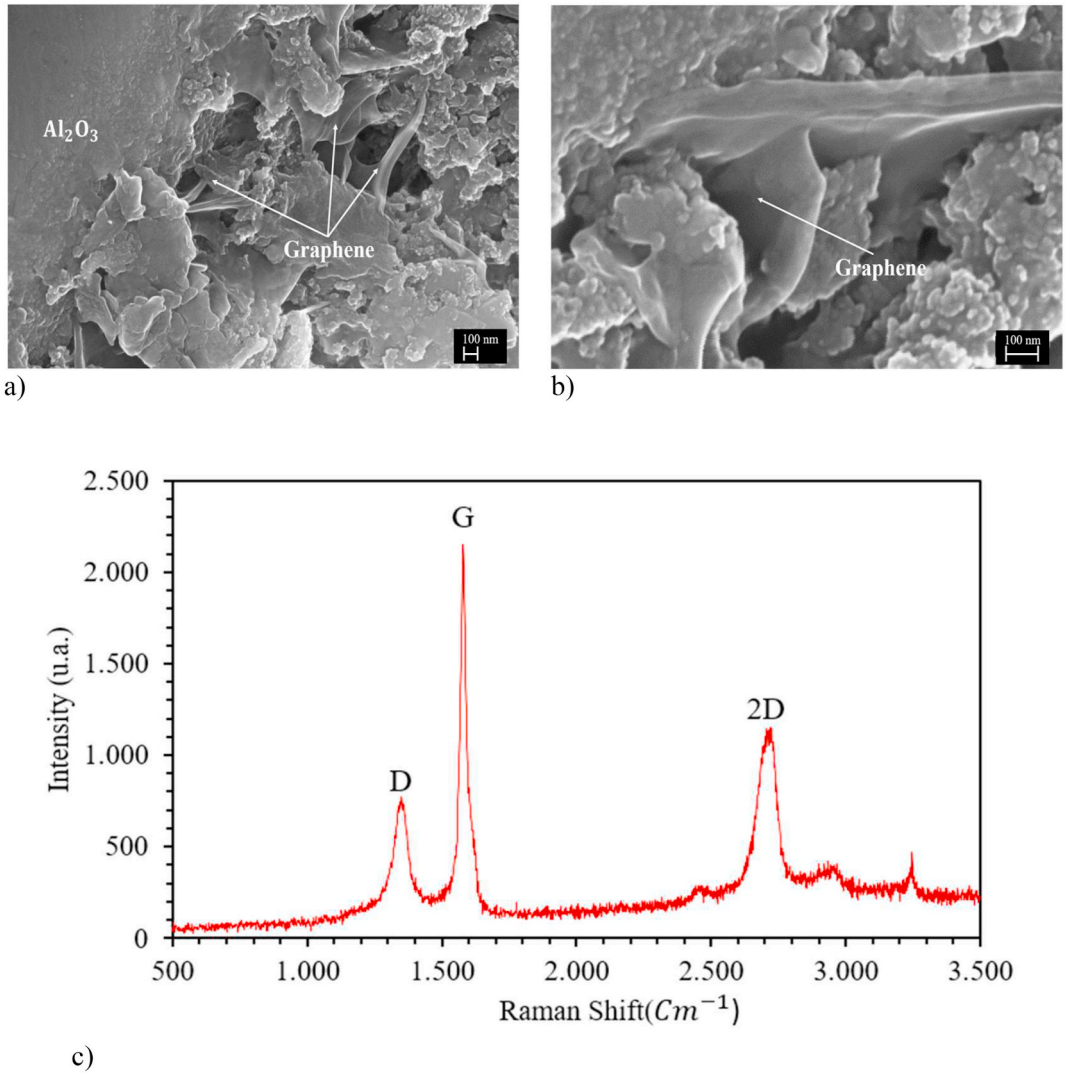

Fig. 7. a) SEM micrographs of GNPs embedded in the Al_2O_3 matrix of Al_2O_3/3%TiO_2 + 3 % coating. b) detail of graphene localization and c) Raman spectra of pure graphene (D, G and 2D bands) acquired on the Al_2O_3/3 % TiO_2/3 % graphene coating. Analysis was performed on the cross-section of the polished samples.

approximately 1.15 times higher than that of the unmodified coatings (1284 ± 72 H V) (Fig. 8b). The coating containing 3 % graphene exhibited the highest microhardness. This is because graphene-modified nanostructured Al_2O_3/3 % TiO_2 coatings are denser (lower porosity) [45] and have a higher ability to resist plastic deformation by indentation, which in turn results in higher microhardness values for the Al_2O_3/3 % TiO_2 + 3 % graphene coatings.

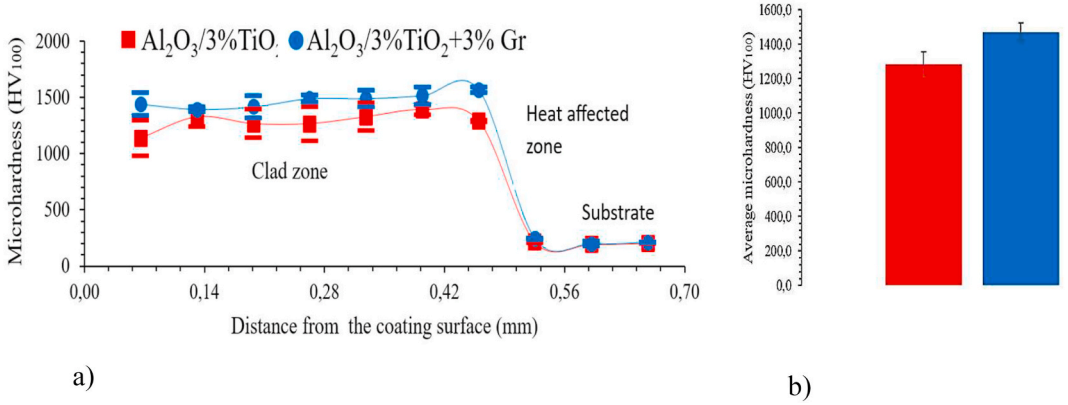

Fig. 8. Microhardness profiles of the deposited ceramic coatings; a) microhardness distribution over the cross section and b) histogram of the average microhardness values.

3.5. Tribological analysis

3.5.1. Friction and wear behaviour

The friction coefficient due to a hard ceramic material sliding on a steel surface with lower hardness is determined based on the deformation during the mutual mechanical interaction between the asperities of the hard ceramic coating surface with the soft steel surface. Because the ceramic sample surface is harder than the steel disc surface, when the ceramic pin is pressed into the steel disc, the asperities of the ceramic pin coating surface may penetrate and plough the steel disc surface and produce grooves at the sliding contact interface if the shear strength is exceeded.

Fig. 9 shows the friction coefficient evolution of the nanostructured Al_2O_3/3 % TiO_2 and Al_2O_3/3 % TiO_2 + 3 % graphene nanoplatelet-deposited coatings against conventional hardened and tempered F-5220 steel discs. Both coatings exhibit the same trend: initially, the friction coefficient reaches a peak value, then suddenly declines, fluctuates, and subsequently stabilises at a certain value. The initial friction coefficients of the unmodified and modified coatings were higher than 0.123 and 0.112, respectively. After a rapid increase (running-in period), the friction coefficient increased to 0.124 for Al_2O_3/3 % TiO_2 + 3 % graphene and to 0.145 for Al_2O_3 + 3 % TiO_2 (secondary stage). For the coating containing 3 % graphene, the friction coefficient curve rapidly reached a stable state after a short run-in period (78 s). The friction coefficient of the unmodified coating reached a steady state at approximately 117 s, which is an increase of over 48 % compared with that of the modified coating. After 3800 s, scratches were observed on the steel disc as a series of grooves parallel to the sliding direction. The increase in the friction coefficient in the first stage could be attributed to the shear deformation of the contact point between the nanostructured Al_2O_3/3 % TiO_2 and the steel disc and/or friction from scraping a trench on the surface. Furthermore, the addition of 3 % graphene to Al_2O_3/3 % TiO_2 drastically reduced the friction coefficient between the friction pairs. This reduction possibly occurs because of the low shear and highly protective nature of graphene. Additionally, the synergistic effect between graphene and the liquid lubricant used in this study could improve the rheological characteristics and wettability of the lubrication layer, which may enhance the interfacial separation between the ceramic coating and steel counterfaces [46]. Many other advantages are derived from the high thermal conductivity, chemical reactivity, excellent mechanical strength, low surface energy, atomic smooth surface, and load transfer of graphene; consequently, the microstructure and properties of nanostructured Al_2O_3/3 % TiO_2-based friction materials are substantially improved [47]. Additionally, the dispersion of graphene in the alumina matrix improves the bonding strength with the lubricating oil, which can considerably affect the tribological properties of the friction pairs. Furthermore, during the friction process, graphene nanoplatelets can be attached to asperities and friction-induced defects to repair worn surfaces and improve the tribological properties. Moreover, the elevated pressure and temperature in the interface during the friction process cause graphene to break into small fragments, which facilitate the mending of grooves and local pits, thereby promoting the repair effect [48].

As shown in Fig. 9, the energy dissipation (tribocontact friction losses) should exhibit an inversely proportional relationship with graphene addition. According to Chen et al. [49], the energy dissipation during the friction test can be evaluated as follows:

$$E = F_n \bullet v \int \mu \, v \, dt$$

where F_n is the applied friction load (20 N), v is the linear velocity (0.07 m/s), and μ is the average kinetic friction coefficient during a travel time of 3800 s. As shown in Fig. 7, the energy consumed by the unmodified coating was 771 J; after adding 3 % graphene, the energy consumed was reduced to approximately 662 J.

Regarding the wear behavior, Fig. 10a and b displays the wear rate as a function of sliding distance. It can be observed that the addition of 3 % of GNPs to nanostructured Al_2O_3/3 % TiO_2 lowered the average wear rate of the ceramic pin by about ~46 % (changing from 3.49 E^{-04} ± 8.47 E^{-05} to 1.90 E^{-04} ±4.32 E^{-05} mm^3/Nm), and the counterpart steel disc by approximately 18 % (changing from 3.57 E^{-03} ± 6.84 E^{-04} to 2.93 E^{-02} ± 5.55 E^{-04} mm^3/Nm). This result shows that the modified coating possesses the most excellent anti-wear performance compared to the non-modified coating. That is because the thin graphene sheets allow good adsorption on the rubbing surfaces, greatly improving friction reduction and anti-wear abilities. These results evidence that the tribosystem evolved from severe (nonmodified coating) to mild (modified) wear by introducing just 3 wt% of GNPs fillers into nanostructured Al_2O_3/TiO_2 ceramic matrices [24].

The surface morphologies, characterized by SEM and optical microscopy (OM), of wear tracks of ceramic coatings and the steel disc are shown in Fig. 10 c and d, respectively. It can be observed that the wear track width has been reduced with the addition of 3 % GNPs. The worn surfaces of nanostructured Al_2O_3/3 % TiO_2 coating and the counterpart steel disc acquired denser wear scars and grooves, dominated by an three-body abrasive wear mechanisms, while the worn surface of

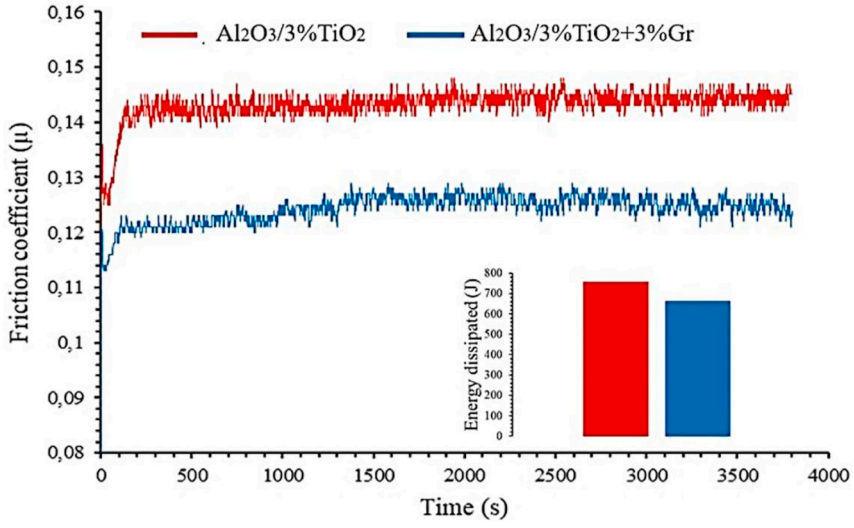

Fig. 9. Friction coefficient evolution of Al_2O_3/3 % TiO_2 and Al_2O_3/3 % TiO_2 + 3 % graphene coatings deposited against F-5220 hardened and tempered steel under lubrication conditions and energy dissipation during friction tests.

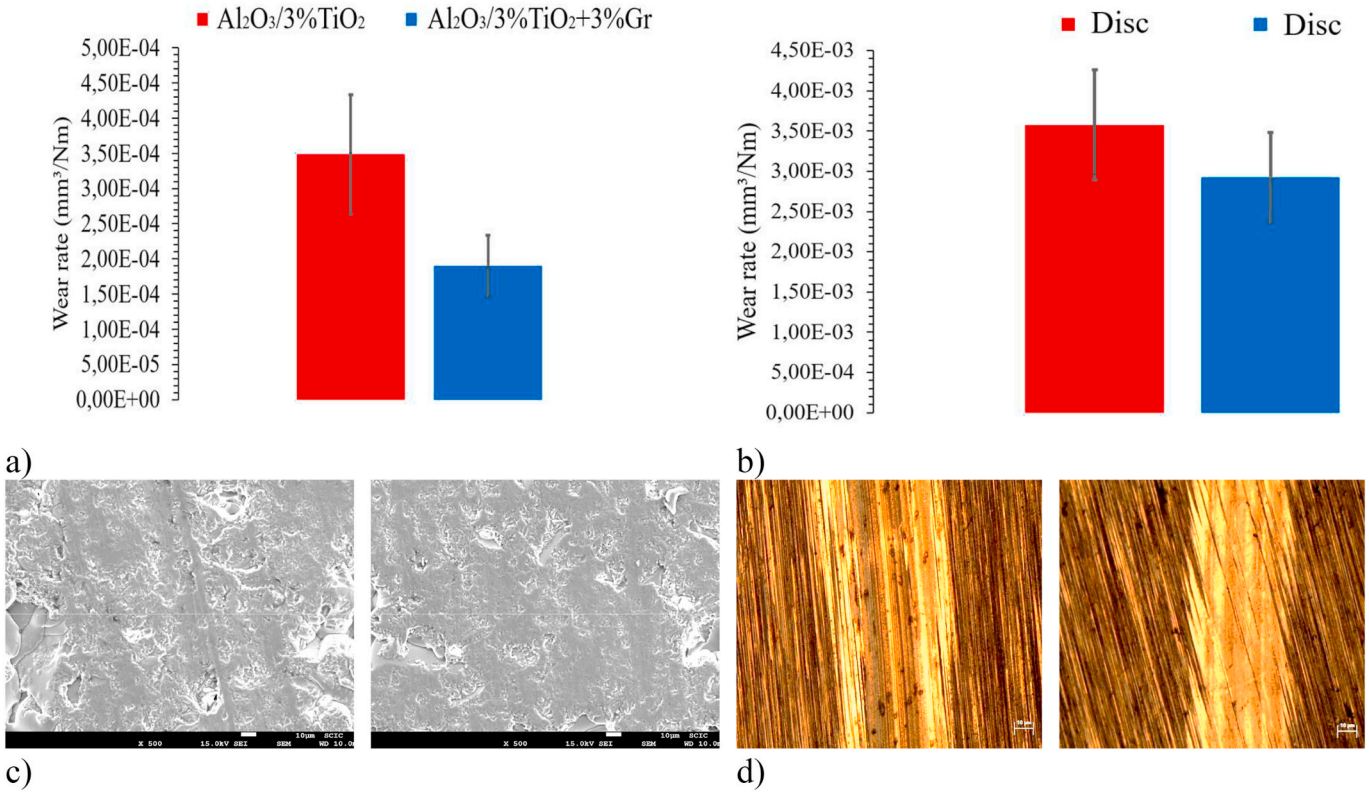

Fig. 10. Average wear rate variation of a) nanostructured Al_2O_3/3 % TiO_2 and b) Counterpart steel discs, c) SEM micrographs of Al_2O_3/3 % TiO_2 composite without and with 3 % GNPs reinforcement coatings and d) optical micrographs of discs wear track.

nanostructured Al_2O_3/3 % TiO_2 + 3 % GNPs appears smaller and has a smoother wear scar. The surface damage of the steel disc may be attributed to the particles (debris size) generated in the friction process, showing scratches consistent with the sliding direction. The wear mechanism dominated by abrasive wear provides greater friction resistance of modified coating, thus decreasing the friction coefficient and wear rate.

3.5.2. *Investigation of lubrication regimes using the stribeck curve*

The Stribeck curve plays a fundamental role in identifying the transition between different lubrication regimes: boundary, mixed, elastohydrodynamic, and hydrodynamic. This curve plots the friction coefficient, and μ is expressed as a function of the non-dimensional Hersey number (H_s), which only includes the operating parameters; ($H_s = \eta . v/P_a$), where η, v, and P_a denote the dynamic viscosity, speed, and apparent stress, respectively.

The results of the friction experiments are shown in Fig. 11. This test was used to evaluate the tribological performances of nanostructured Al_2O_3/3 % TiO_2 and Al_2O_3/3 % TiO_2 + 3 % graphene under different conditions. Both coatings demonstrated a decrease in the friction coefficient with H_s, revealing fluid film entrainment and the formation of a partial hydrodynamic film until the friction coefficient reached a minimum value. The coatings clearly showed the minimum value of the friction coefficient, indicating the transition between full fluid-film

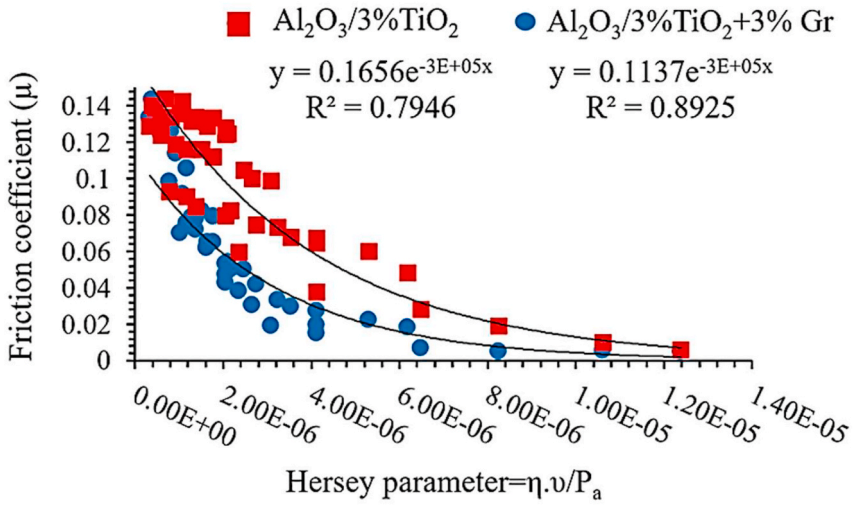

Fig. 11. Stribeck curves of OF-deposited Al_2O_3/3 % TiO_2 and Al_2O_3/3 % TiO_2 + 3 % graphene with transitions from BL to ML regimes.

lubrication and some solid asperity interactions (ML regime). BL conditions corresponded to low values of H_s, whereas full film lubrication conditions occurred at high H_s values (EHL); the intermediate values corresponded to ML. Transitions between the lubrication regimes of the unmodified coating (nanostructured Al_2O_3/3 % TiO_2) occurred at $H_s = 3.09 \times 10^{-6}$ for BL–ML under 12 N load at 0.21 m/s with a friction coefficient of 0.1. The maximum value of H_s was 1.24×10^{-5} under 3 N load at 0.21 m/s with a friction coefficient of 0.006, whereas the transition from BL to ML for (nanostructured Al_2O_3/3 % TiO_2 + 3 % graphene) occurred at $H_s = 7.86 \times 10^{-7}$ under 9 N load at 0.04 m/s with a friction coefficient of 0.1. The maximum value of H_s was 1.24×10^{-5} under 3 N load at 0.21 m/s with a friction coefficient of 0.005.

Both Stribeck curves have a typical shape with three lubrication regimes can be identified and a well-developed minimum friction coefficient value that is consider to divide the elastohydrodynamic (EHL) from the mixed (ML) and boundary lubrication (BL) regimes. The position of the minimum in each curve is similar within the experimental error and shows that the presence of graphene in Al_2O_3/3 % TiO_2 does not influence the transition positions on the H_s axis. The optimal results in terms of the friction coefficient reduction are obtained for samples of nanostructured Al_2O_3/3 % TiO_2 + 3 % graphene. The friction coefficient values are affected by the detachment of graphene nanoplatelets from the ceramic coating to the oil lubricant, which can lead to the formation of a continuous lubrication layer that can separate the contact surfaces; furthermore, a tribofilm is formed owing to the interaction between the graphene molecules and the contact surfaces [50].

Based on the above analyses, the nanostructured Al_2O_3/3 % TiO_2 + 3 % graphene coating exhibits excellent tribological characteristics owing to the presence of a well-covered lubricating layer and graphene transfer films on the surface of the friction pairs (ceramic pin and metallic disc). The formation of the lubricating layer and graphene transfer films during sliding may proceed as follows:

a) During the initial stages of sliding, a linearly decreasing slope (negative) is observed between the friction coefficient and H_s in the BL zone (Fig. 12a); the surface asperities of the Al_2O_3/3 % TiO_2 and Al_2O_3/3 % TiO_2 + 3 % graphene coatings rapidly separate under an extremely high initial contact pressure and low speed, resulting in the formation of wear debris particles. In the subsequent sliding cycles, most of the wear particles are accumulated in the pores of the coating, and the pull-out graphene (modified coating) in the smaller pores and grain boundaries is released at the friction interface. Meanwhile, a portion of the GNPs is transferred to the frictional pin ceramic and metallic disc surfaces. For the modified coating with a lower pore size distribution, a fraction of the detached graphene is distributed over the contact surfaces, forming a tribofilm, and the remaining fraction is dispersed in the lubricating oil because of the synergistic effect of the graphene nanoplatelets. Consequently, the modified coating exhibits an enhanced tribological performance.

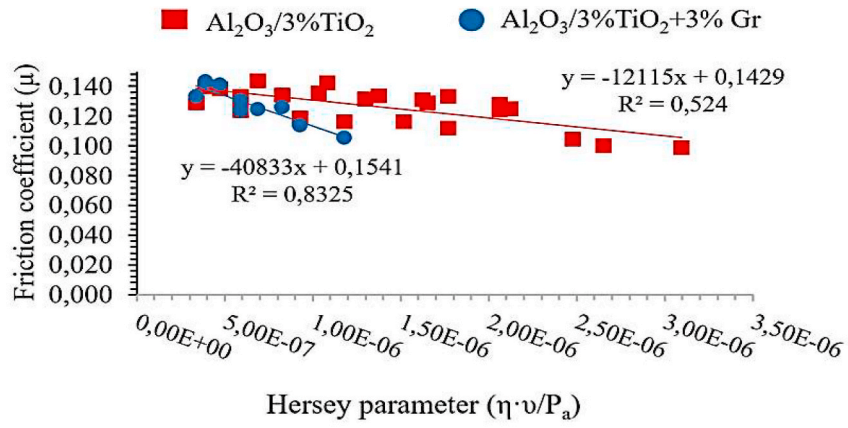

a)

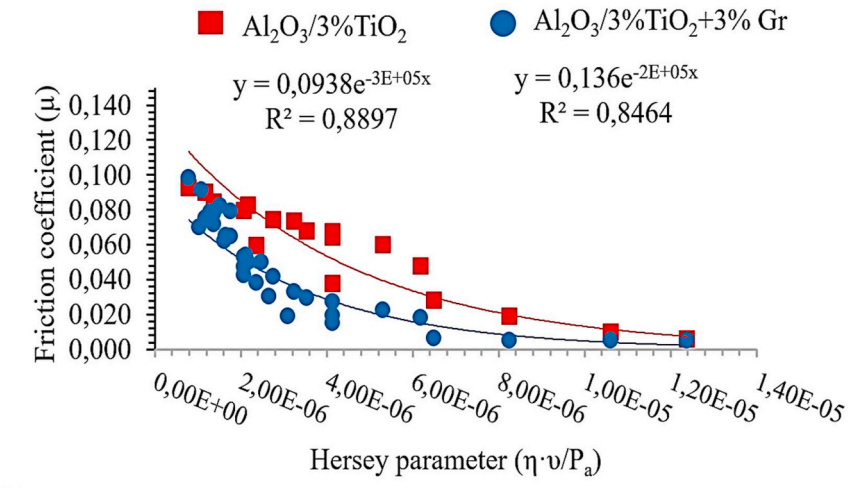

b)

Fig. 12. Detail of the Stribeck curve: a) BL zone (negative linear slope) and b) ML zone (exponential trendline).

b) The higher H_s value in the BL zone corresponding to the unmodified coating indicates the effect of the wear debris size on abrasive wear. When the wear debris size is larger than the roughness of the sliding surface, abrasive wear occurs owing to the wear debris and an insufficient lubrication effect, thereby increasing the friction force. However, when the wear debris size is smaller than the roughness of the sliding surface, as observed in the modified coating, rolling of wear debris occurs because the wear debris with the graphene film is not attached to the two contact surfaces, thereby decreasing the friction coefficient [51,52], reducing the H_s number, and increasing the negative slope of the linear function in this zone. The interlaminar (interface) shear slip (shear stress τ) is considered more likely to occur in graphene platelet, consequently improving the friction reduction and reducing the Hs value. Detected graphene with a smaller particle size is less prone to structural defects and wrinkles and is more easily adsorbed on the sliding surface to form a lubricating film [53] and also on wear debris particles, providing enhanced wear (surface roughness) and frictional performance.

c) The high hardness (high resistance to plastic deformation) of the modified nanostructured ceramic coating reduces the probability of producing cracks or other debris after the detachment of asperities and GNPs, which is significant for generating and improving lubricating films.

d) Through repeated sliding conditions and friction-induced localized heat at the interface (flash temperature), the large wear debris is reduced to the nanoscale and enters the lubricating film together with the GNPs. This can appreciably enhance the strength of the film and enable the formation of a converging gap between the two contacting surfaces into which the lubricant oil is drawn. Consequently, a pressure field can be created to support the applied load and separate the friction pairs, resulting in a sudden decline (exponential trendline) in the friction coefficient (ML zone) (Fig. 12b). Additionally, the detached graphene platelets that adhere to the Al_2O_3/3 % TiO_2 pin and metallic disc surfaces are continuously graphitised, thus providing excellent solid lubrication.

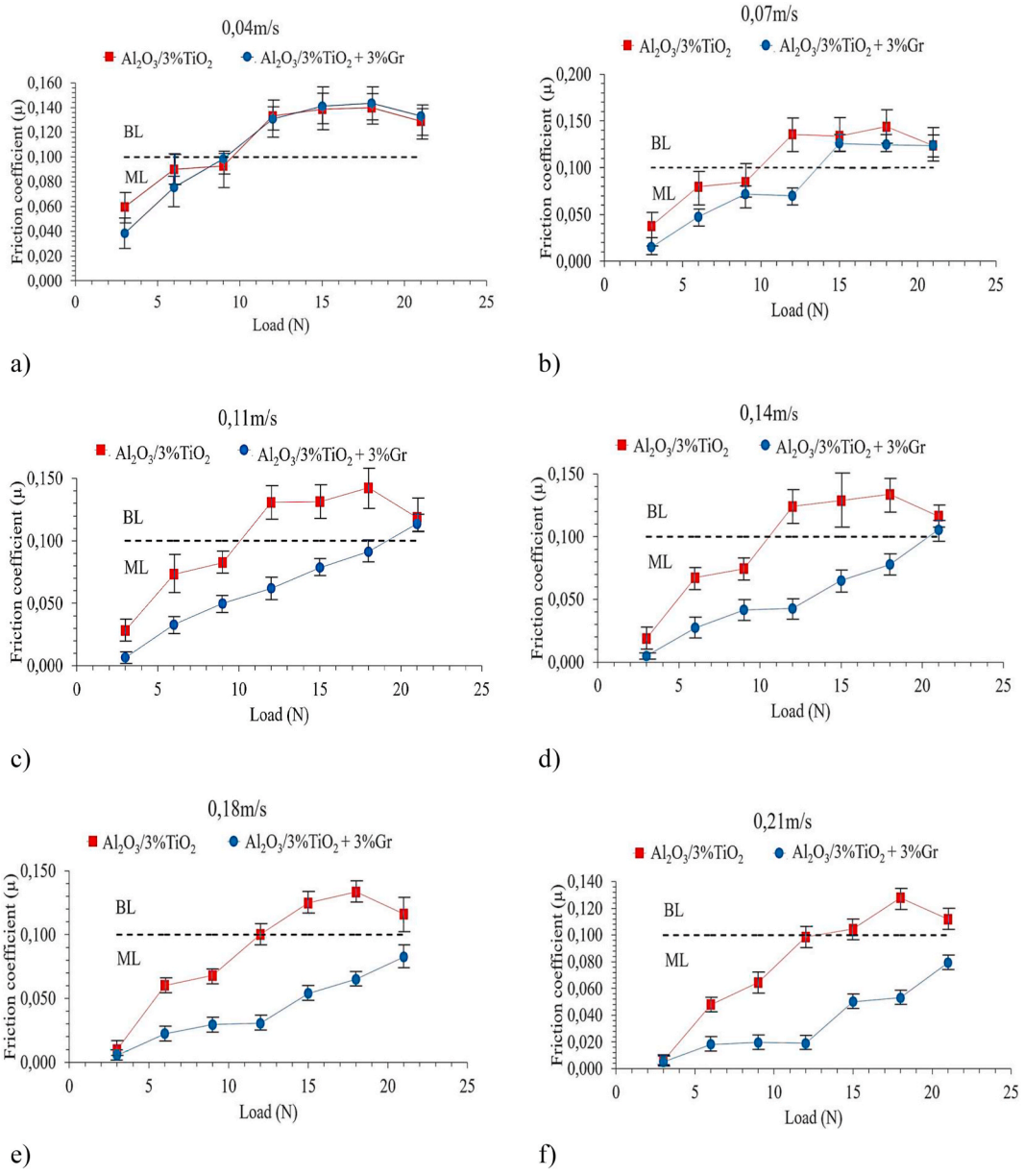

Fig. 13. Behaviour of the friction coefficient as a function of the applied load at various sliding speeds and the critical condition for the transition from BL to ML for Al_2O_3/3 % TiO_2 and Al_2O_3/3 % TiO_2 + 3 % graphene.

3.5.3. Critical condition for the transition from BL to ML

Based on a previous study [54], we considered that the transition from BL to ML regimes occurs at a definite value of the friction coefficient (0.1). The parameters that were measured to assess the tribological performance of the nanostructured Al_2O_3/3 % TiO_2 coating and the modified coating containing nanographene included the friction coefficient and the critical load at a fixed speed of the transition from BL to ML regimes for the ceramic coatings. To study the effects of the load and speed on the tribological parameters at the pin/disc interface, the load was varied from 3 to 21 N to clarify the lubrication regimes.

The variations in the friction coefficient (μ) and lubrication regime, as functions of the applied load at each speed, are plotted in Fig. 13, which depicts the change in the lubrication regime as the load increases under a constant speed. To clarify the effect of graphene addition to Al_2O_3/3 % TiO_2 on the transition between lubrication regimes, the average friction coefficient was calculated by calculating the average value of all instantaneous friction coefficients when the friction was relatively stable. The lubrication regimes that graphene could provide for contact friction pairs of nanostructured Al_2O_3/3 % TiO_2 and Al_2O_3/3 % TiO_2 + 3 % graphene versus hardened and tempered F-5220 discs were observed.

The friction coefficients versus applied loads at a sliding speed of 0.04 m/s are shown in Fig. 13a. At higher loads (12, 15, 18, and 21 N), both coatings can only enter the BL regimes with approximately similar friction coefficient values, and the critical load for the transition from BL to ML is approximately 9 N, because the friction coefficient decreases gradually when the applied load is lower than this value. This is because the contact stress of the frictional pairs is exceedingly high under high loads, and a partial fluid film cannot be easily formed owing to the inadequate viscosity of the oil lubricant. In the ML regime, the lubrication properties of the modified coating (Al_2O_3/3 % TiO_2 + 3 % graphene) are slightly higher than those of the unmodified coating (Al_2O_3/3 % TiO_2), indicating a lower friction coefficient. This is because the incorporation of detached graphene and nano alumina debris particles can be increases the viscosity of the lubricant oil film in the interface between the friction pairs [55,56], thereby decreasing the friction coefficient and improving the tribological performance of lubricants oil.

As shown in Fig. 13b, upon increasing the sliding speed to 0.07 m/s, the unmodified coating nearly maintains its friction values in the BL zone under loads of 12, 15, 18, and 21 N, although the critical load for the transition from BL to ML is approximately 9.5 N. However, the friction coefficient of the graphene-modified coating decreases in the BL zone under loads of 15, 18, and 21 N, and the critical load for the transition from BL to ML is approximately 13.5 N. The remaining loads and resulting friction values correspond to the ML regime.

As shown in Fig. 13c and d, the critical loads for the transition from BL to ML for the unmodified coating, within the sliding speed range of the tests (0.11 and 0.14 m/s), are approximately 10 and 11 N, respectively. In contrast, for the modified coating, the friction pairs can enter the ML regime under critical loads of 19 and 20.5 N.

Under sliding speeds of 0.18 and 0.21 m/s, the critical load for the transition is approximately 12.5 N for the unmodified coating. However, the modified coating demonstrates that the friction coefficient decreases as the sliding speed increases, and the lubrication regime gradually changes from BL to ML under all applied loads, (Fig. 13e and f). This is because the incorporation of graphene into the oil lubricant substantially improves the lubrication performance of the friction pairs owing to its ability to form a boundary film [57], thus reducing the friction coefficient, enhancing heat dissipation, and optimising load distribution. Furthermore, the microscopic interactions between graphene and liquid lubricating oil molecules markedly affect the rheological and tribological properties of the solid–liquid lubricating system [58]. Graphene can be stably adsorbed (or can interact with a smooth surface) on rubbing surfaces lubricated by a base oil, which confirms that graphene can form a physical deposition film on rubbing surfaces [59].

In addition to the lower friction coefficient obtained with the graphene-containing nanostructured Al_2O_3/TiO_2 compared with that of the unmodified nanostructured Al_2O_3/TiO_2 coating under all the tested conditions, a major difference is the formation of a lubricant layer with improved stability and continuity; moreover, the applied load is completely supported by the thin lubricant layer, where the bulk property of the lubricant and entrainment velocity of the tribo-pairs determine the film thickness and friction coefficient. The enhancement of the dispersity and stability of the lubricant layer is crucial for its tribological performance and unique functionality, thus improving the longevity and energy conservation of industrial components. The testing results (Fig. 13a–f) indicate that, with the modified ceramic coating, a continuous lubricant film with a higher load-carrying capacity is only formed under severe test conditions (higher loads and lower velocities).

To better understand the difference in the tribological behaviour, we studied the surface roughness evolution of the worn surfaces of the deposited coatings after a distance of 600 m (Table 4). The addition of graphene nanoplatelets to the nanostructured Al_2O_3/3 % TiO_2 reduces the material removal of the friction pairs and the root mean square of the surface roughness of the contacting surfaces. This is because the addition of 3 % graphene to Al_2O_3/3 % TiO_2 results in the lowest surface roughness of both the ceramic pin and metallic disc, indicating that the addition of graphene improves the wear resistance of the coating. A previous study [60] demonstrated that cracks could scarcely penetrate graphene because of its strength. When the graphene is adequately separated in the coating, some cracks are blocked by GNPs or the pathway is changed. This prevents the coating from prematurely spalling. The decrease in debris size results in a low surface roughness of the friction pairs. The higher scratching (surface roughness) observed in the friction pair of the unmodified nanoceramic coating/metallic steel disc can be attributed to the low motion of debris particles [61,62]. The effect of debris on the tribological behaviour depends on the size variation and wear debris distribution [63].

In order to explain the mechanisms that take place during the tribological process, as well as the role played by the addition of graphene in the friction coefficient, the worn surfaces were analysed by EDX techniques. In terms of friction, there is a general consensus that relates the better friction performance of ceramic/graphene composites with the formation of a lubricant carbon-rich tribofilm. In the present work, the presence of this tribolayer was also confirmed, by SEM microscopy. Fig. 14a and b, shows that under high applied loads and localized heat (flash temperature) during friction test, graphene sheets from nanoplatelets are pulled under shear (exfoliation) and become interacted with overlapping friction surfacing to form an ultrathin graphene tribofilm (spot 1). The composition of this layer was fundamentally based on carbon. Likewise, it also contained ceramic elements (from the Al_2O_3 matrix (spot 2 and the steel debris counterbody (spot 3), Fig. 14c, since, during the sliding process, the carbonaceous and ceramic debris mix and compact to form tribofilm, which serves both as a solid lubricant and as a protecting film and reduces the friction coefficient. These results are in quite good agreement with the previously reported mechanism for the tribofilm formation during friction process [64–67].

Raman spectroscopy was used to confirm that this excellent tribological behavior of the modified coating is attributed to the presence of graphene and alumina debris particles in the lubricant oil Fig. 15a, confirming the combination of alumina and graphene within the lubricated oil. Al_2O_3 shows peaks ranging from 200 to 1200 cm^{-1}. Peaks at 360, 502, 899, 1094 and 1118 are identical to the established data,

Table 4
Final surface roughness of ceramic pins and disc after tribology tests.

Coatings	Pin final R_a (nm)	Disc final R_a (nm)	Final σ $(R^2_{a\_pin}+R^2_{a\_disc})^{1/2}$
Al_2O_3/3%TiO_2	875	683	1110
Al_2O_3/3% TiO_2+3%Gr	622	516	808.2

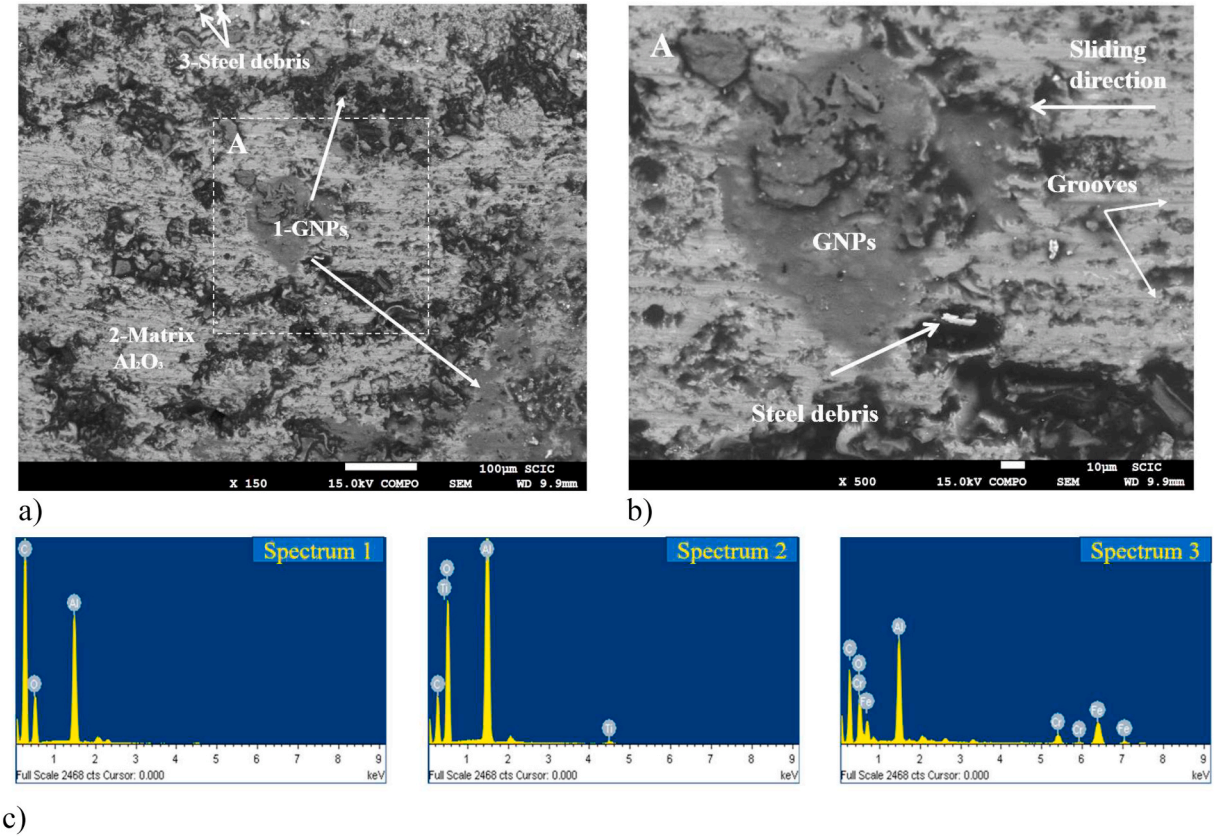

Fig. 14. SEM analysis of the tribofilm formed on the Al_2O_3/TiO_2 + 3 % graphene composite. SEM micrographs of: a) Tribofilm formed in different zones of wear track; b) magnified view of tribofilm and c) EDS spectra taken in various positions.

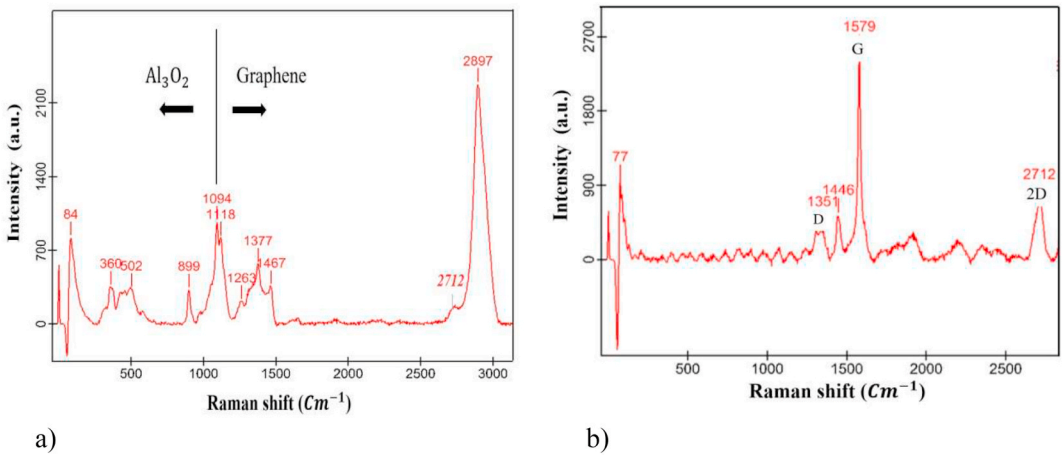

Fig. 15. Characterization results of nanomaterials used, Raman spectra, for; a) $Al_2O_3/3\%TiO_2/G$ and b) graphene containing oil suspension.

which confirms that the material is Al_2O_3. The bands that appeared between 240 and 500 cm^{-1} is associated with Al–O vibration stretching and the high intensity bands above 500 cm^{-1} arise from the stretching of hydroxyl groups. Moderate and low-intensity bands appear in the same range indicating deformation of hydroxyl groups [68]. Graphene is represented by the bands at 1351, 1579, and 2712 cm^{-1}, Fig. 15b. The characteristic peaks at D-band and G-band, are the main features of sp^2 crystalline graphitic structures and confirm their presence in modified composites. While the D peak second order changes in shape, width, and position for an increasing number of layers, reflecting the change in the electron bands via a double resonant Raman process.

4. Conclusions

1. The tribological advantages of $Al_2O_3/_3$ % TiO_2 + 3 % graphene nanoplatelets were clearly demonstrated through various tribology tests, such as Stribeck curve analysis, friction testing at constant sliding speeds and applied loads, energy dissipation measurements during friction tests, and determination of the critical load-carrying capacity for the transition from BL to ML at various sliding speeds. The experimental results revealed a 3.8 time reduction in porosity contain, an approximately 15 % increase in the average microhardness of the modified ceramic top layer and a decrease of 16.5 % in the steady-state. The significant reduction in friction coefficient suggests

the great potential of adding graphene nanoplatelets as an energy-saving approach.

2. Although the phase volume ratio is practically the same between both coatings, the graphene modified nanostructured Al_2O_3/3 % TiO_2 coatings exhibited higher hardness due to their lower porosity content.
3. The dispersion stability and tribological enhancement of the modified coating could be attributed to several factors, including the use of nanosized alumina particles, the inclusion of pristine detached graphene as an additive in oil-based lubricants, and the synergistic interaction between alumina and graphene nanoplatelets in combination with lubricating oil. The incorporation of graphene decreased the H_s number by up to 61 %, whereas it increased the critical load capacity for the transition from BL to ML regimes by enhancing the composition and strength of the lubricant film. These improvements are crucial for satisfying the industrial requirements for higher loads, lower sliding speeds, and enhanced performance expectations in various engineering applications that emphasise sustainability and energy savings.
4. The wear properties of the nanostructured Al_2O_3/TiO_2 coating can be significantly improved through the addition of 3 % GNPs. The comparison of non-modified and modified ceramic-based coatings reveals that the modified coating reduces wear rates by forming a tribo-film and absorbing stress. The interaction between GNPs with the friction pairs and its synergistic role with the oil lubricant significantly reduces wear rates in modified coatings.
5. Further investigation is necessary to examine the critical load-carrying capacity for the transition from BL to ML and the interactions between the graphene nanoplatelets, lubricant film, and/or lubricant additives. This comprehensive exploration can facilitate the formulation of new lubricants and the design of robust tribological components to effectively integrate lubricant and ceramic coating technologies. This integration is essential for achieving optimal performance in specific industrial applications. Consequently, the properties of new materials can be optimally designed and controlled.

CRediT authorship contribution statement

K.A. Habib: Investigation. **D.L. Cano:** Investigation. **J. Serrano-Mira:** Software. **Emilio Rayón:** Software. **José V. Abellán-Nebot:** Investigation. **S. Dosta:** Investigation.

Declaration of competing interest

The authors declare that they have no known competing financial interests or personal relationships that could have appeared to influence the work reported in this paper.

Data availability

No data was used for the research described in the article.

Acknowledgments

• MGS (David Leal Cano) supported by the Margarita Salas post-doctoral contract MGS/2021/10 (UP2021-021) financed by the European Union-NextGenerationEU.

• This research was funded by by MCIN/AEI/10.13039/501100011033 through PID-AEI Project (grant PID2021-123753NA-C33), and, as appropriate, by "ERDF A way of making Europe", by the "European Union" or by the "European Union NextGenerationEU/PRTR"

References

[1] P. Hvizdoš, J. Dusza, C. Balázsi, Tribological properties of Si_3N_4–graphene nanocomposites, J. Eur. Ceram. Soc. 33 (12) (2013) 2359–2364.
[2] H. Li, Study on Tribological Behavior and Cell Compatibility of Graphene Reinforced Ceramic Matrix Composite Coatings, University of Chinese Academy of Sciences, 2014.
[3] Y. Wang, S. Jiang, M. Wang, S. Wang, T.D. Xiao, P.R. Strutt, Wear 237 (2000) 176–185.
[4] M. Gell, E.H. Jordan, Y.H. Sohn, D. Goberman, L. Shaw, T.D. Xiao, Development and implementation of plasma sprayed nanostructured ceramic coatings, Surf. Coating. Technol. 146 (2001) 48–54.
[5] E.H. Jordan, M. Gell, Y.H. Sohn, D. Goberman, L. Shaw, S. Jiang, P. Strutt, Fabrication and evaluation of plasma sprayed nanostructured alumina–titania coatings with superior properties, Mater. Sci. Eng. 301 (1) (2000) 80–89, 1.
[6] D. Goberman, Y.H. Sohn, L. Shaw, E. Jordan, M. Gell, Microstructure development of Al_2O_3–13wt.% TiO_2 plasma sprayed coatings derived from nanocrystalline powders, Acta Mater. 50 (5) (2002) 1141–1152.
[7] Y. Wang, C. Li, L. Guo, W. Tian, Laser remelting of plasma sprayed nanostructured Al_2O_3–TiO_2 coatings at different laser power, Surf. Coating. Technol. 204 (21–22) (2010) 3559–3566.
[8] B. Pietrzyk, S. Miszczak, Y. Sun, M. Szymański, Al_2O_3 + graphene low-friction composite coatings prepared by sol–gel method, Coatings 10 (9) (2020) 858.
[9] Z. Zou, Y. Wang, F. Zhou, L. Wang, S. Liu, Y. Wang, Tribological property of plasma sprayed Al_2O_3-13wt%TiO_2 coatings onto resin-based composites, Appl. Surf. Sci. 431 (2018) 75–80.
[10] G.L. Li, J.L. Ma, H.D. Wang, J.J. Kang, B.S. Xu, Effects of argon gas flow rate on the microstructure and micromechanical properties of supersonic plasma sprayed nanostructured Al_2O_3-13wt.%TiO_2 coatings, Appl. Surf. Sci. 311 (2014) 124–130.
[11] H.M. Bian, Y. Yong, W. You, T. Wei, Preparation of nanostructured alumina–titania composite powders by spray drying, heat treatment and plasma treatment, Powder Technol. 219 (2012) 257–263.
[12] Z.S. Wu, G. Zhou, L.C. Yin, W. Ren, F. Li, H.M. Cheng, Graphene/metal oxide composite electrode materials for energy storage, Nano Energy 1 (1) (2012) 107–131.
[13] F. Khodabakhshi, M. Nosko, A.P. Gerlich, Effects of graphene nano-platelets (GNPs) on the microstructural characteristics and textural development of an Al-Mg alloy during friction-stir processing, Surf. Coating. Technol. 335 (2018) 288–305.
[14] C. Liu, J. Sun, F. Venturi, A.R. Romero, T. Hussain, Enhancing wear performance by depositing alumina/GNPs coating on textured WC-TiC-Co, Surf. Coating. Technol. 447 (2022) 128817.
[15] F. Ren, G.M. Zhu, P.G. Ren, The latest advances in preparation and application of nano graphene composites, Acta Mater. Compos. Sin. 31 (2) (2014) 263–272.
[16] H.S. Dong, S.J. Qi, Realising the potential of graphene-based materials for biosurfaces–A future perspective, Biosurface and Biotribology 1 (4) (2015) 229–248.
[17] L. Qin, D. Bian, Y. Zhao, X. Xu, Y. Guo, Study on the preparation and mechanical properties of alumina ceramic coating reinforced by graphene and multi-walled carbon nanotube, Russ. J. Appl. Chem. 90 (2017) 811–817.
[18] A. Nieto, J.M. Zhao, Y.H. Han, K.H. Hwan, J.M. Schoenung, Microscale tribological behavior and in vitro biocompatibility of graphene nanoplatelet reinforced alumina, J. Mech. Behav. Biomed. Mater. 61 (2016) 122–134.
[19] H. Li, Y. Xie, K. Li, L. Huang, S. Huang, B. Zhao, X. Zheng, Microstructure and wear behavior of graphene nanosheets-reinforced zirconia coating, Ceram. Int. 40 (8) (2014) 12821–12829.
[20] B. Yazdani, F. Xu, I. Ahmad, X. Hou, Y. Xia, Y. Zhu, Tribological performance of Graphene/Carbon nanotube hybrid reinforced Al_2O_3 composites, Sci. Rep. 5 (1) (2015) 11579.
[21] A. Gómez-Gómez, A. Nistal, E. García, M.I. Osendi, M. Belmonte, P. Miranzo, The decisive role played by graphene nanoplatelets on improving the tribological performance of Y_2O_3-Al_2O_3-SiO_2 glass coatings, Mater. Des. 112 (2016) 449–455.
[22] D. Bian, T.V. Aradhyula, Y. Guo, Y. Zhao, Improving tribological performance of chemically bonded phosphate ceramic coatings reinforced by graphene nano-platelets, Ceram. Int. 43 (15) (2017) 12466–12471.
[23] Javier Llorente, Manuel Belmonte, Rolled and twisted graphene flakes as self-lubricant and wear protecting fillers into ceramic composites, Carbon 159 (2020) 45–50.
[24] Javier Llorente, Cristina Ramírez, Manuel Belmonte, High graphene fillers content for improving the tribological performance of silicon nitride-based ceramics, Wear 430 (2019) 183–190.
[25] A. Kulkarni, S. Sampath, A. Goland, H. Herman, B. Dowd, Computed microtomography studies to characterize microstructure-property correlations in thermal sprayed alumina deposits, Scripta Mater. 43 (5) (2000) 471–476.
[26] L.L. Shaw, D. Goberman, R. Ren, M. Gell, S. Jiang, Y. Wang, T.D. Xiao, P.R. Strutt, The dependency of microstructure and properties of nanostructured coatings on plasma spray conditions, Surf. Coat. Technol. 13 (2000) 1–8.
[27] M. Woydt, R. Wäsche, The history of the Stribeck curve and ball bearing steels. The role of Adolf Martens, Wear 268 (11–12) (2010) 1542–1546.
[28] A. Rico, J. Rodriguez, E. Otero, P. Zeng, W.M. Rainforth, Wear behaviour of nanostructured alumina–titania coatings deposited by atmospheric plasma spray, Wear 267 (5–8) (2009) 1191–1197.
[29] X. Lin, Y. Zeng, C. Ding, P. Zhang, Effects of temperature on tribological properties of nanostructured and conventional Al_2O_3–3 wt.% TiO_2 coatings, Wear 256 (11–12) (2004) 1018–1025.

[30] F. Ahmed, M.A. Abir, P.K. Bhowmik, V. Deshpande, A.S. Mollah, Thermohydraulic performance of water mixed Al_2O_3, TiO_2 and graphene-oxide nanoparticles for nuclear fuel triangular subchannel, Therm. Sci. Eng. Prog. 24 (2021) 100929.
[31] Y. Li, J. Liu, J. Deng, J. He, Y. Qin, Y. Xing, F. Yin, Fabricación de recubrimientos de Al_2O_3 rociados con plasma reforzado con óxido de grafeno, Ceram. Int. 49 (2) (2023) 1667–1677.
[32] D. Goberman, Y.H. Sohn, L. Shaw, E. Jordan, M. Gell, Microstructure development of Al_2O_3–13wt.% TiO_2 plasma sprayed coatings derived from nanocrystalline powders, Acta Mater. 50 (5) (2002) 1141–1152.
[33] J.A. Vreeling, Y.T. Pei, B. Wind, V. Ocelık, J.T.M. De Hosson, Formation of γ-Al_2O_3 in reaction coatings produced with lasers, Scripta Mater. 44 (4) (2001) 643–649.
[34] I. Levin, D. Brandon, Metastable alumina polymorphs: crystal structures and transition sequences, J. Am. Ceram. Soc. 81 (8) (1998) 1995–2012.
[35] S.J. Wilson, The dehydration of boehmite, γ-AlOOH, to γ- Al_2O_3, J. Solid State Chem. 30 (2) (1979) 247–255.
[36] L. Kovarik, M. Bowden, J. Szanyi, Szanyi János, High temperature transition aluminas in δ- Al_2O_3/θ- Al_2O_3 stability range, J. Catal. 393 (2021) 357–368.
[37] C.D. Rabadia, Y.J. Liu, L. Wang, H. Sun, L.C. Zhang, Laves phase precipitation in Ti-Zr-Fe-Cr alloys with high strength and large plasticity, Mater. Des. 154 (2018) 228–238.
[38] L.C. Zhang, Z.Q. Shen, J. Xu, Mechanically milling-induced amorphization in Sn-containing Ti-based multicomponent alloy systems, Mater. Sci. Eng., A 394 (2005) 204–209.
[39] I. Levin, L.A. Bendersky, D.G. Brandon, M. Rühle, Cubic to monoclinic phase transformations in alumina, Acta Mater. 45 (9) (1997) 3659–3669.
[40] P.S. Santos, H.S. Santos, S.P.D. Toledo, Standard transition aluminas. Electron microscopy studies, Mater. Res. 3 (2000) 104–114.
[41] G. Paglia, Determination of the Structure of Y-Alumina Using Empirical and First Principle Calculations Combined with Supporting Experiments (Doctoral Dissertation, Curtin University), 2004.
[42] M.U. Devi, On the nature of phases in Al_2O_3 and Al_2O_3–SiC thermal spray coatings, Ceram. Int. 30 (4) (2004) 545–553.
[43] J.R. Davis, Nickel Cobalt and Their Alloys, ASM Specialty Handbook, ASM International, Ohio, 2000.
[44] T.S. Sidhu, S. Prakash, R. Agrawal, D. Agrawal, Studies of the metallurgical and mechanical properties of high velocity oxy-fuel sprayed stellite-6 coatings on Ni and Fe based superalloys, Surf. Coat. Technol. 201 (1–2) (2006) 273–281.
[45] L. Wang, S. Liu, J. Gou, Q. Zhang, F. Zhou, Y. Wang, R. Chu, Study on the wear resistance of graphene modified nanostructured Al_2O_3/TiO_2 coatings, Appl. Surf. Sci. 492 (2019) 272–279.
[46] A.K. Rasheed, M. Khalid, W. Rashmi, T.C.S.M. Gupta, A. Chan, Graphene based nanofluids and nanolubricants–Review of recent developments, Renew. Sustain. Energy Rev. 63 (2016) 346–362.
[47] S. Chen, Y. Liu, K. Feng, Effects of graphene additions on iron-based friction material prepared from vanadium-bearing titanomagnetite concentrates directly, Metall. Mater. Trans. B 53 (5) (2022) 3334–3343.
[48] Q. Gao, S. Liu, K. Hou, Z. Li, J. Wang, Graphene-based nanomaterials as lubricant additives: a review, Lubricants 10 (10) (2022) 273.
[49] X. Chen, X. Qin, Z. Zhu, K. Gao, Evolución microestructural y propiedades de desgaste de los recubrimientos NiCrBSi de revestimiento de inducción local continua, J. Mater. Process. Technol. 262 (2018) 257–268.
[50] Y. Li, J. Liu, J. Deng, J. He, Y. Qin, Y. Xing, F. Yin, Fabrication of graphene oxide reinforced plasma sprayed Al_2O_3 coatings, Ceram. Int. 49 (2) (2013) 1667–1677.
[51] H.G. Lee, S.S. Kim, Effect of compacted wear debris on the tribological behavior of carbon/epoxy composites, Compos. Struct. 74 (2) (2006) 136–144.
[52] H. Liang, X. Chen, Y. Bu, M. Xu, G. Zheng, K. Gao, J. Zhang, Macroscopic superlubricity of potassium hydroxide solution achieved by incorporating in-situ released graphene from friction pairs, Friction 11 (4) (2023) 567–579.
[53] S. Kong, J. Wang, W. Hu, J. Li, Effects of thickness and particle size on tribological properties of graphene as lubricant additive, Tribol. Lett. 68 (2020) 1–10.
[54] J.A. Brandão, M. Meheux, F. Ville, J.H. Seabra, J. Castro, Comparative overview of five gear oils in mixed and boundary film lubrication, Tribol. Int. 47 (2012) 50–61.
[55] X. Fan, Y. Xia, L. Wang, W. Li, Multilayer graphene as a lubricating additive in bentone grease, Tribol. Lett. 55 (2014) 455–464.
[56] P. Verma, M.S. Charoo, P. Dev Srivyas, T. Medhi, Enhanced extreme pressure and tribological performance of hybrid nano lubricant, Tribol. Mater. Surface Interfac. 17 (3) (2023) 203–216.
[57] F. Qiu, H. Song, W. Feng, Z. Yang, F. Zhang, X. Hu, Molecular dynamics simulations of the interaction between graphene and lubricating oil molecules, Tribol. Lett. 71 (2) (2023) 33.
[58] L. Pan, Y. Han, Y. Chen, L. Guo, Synergistic lubrication effects and tribological properties of graphene/oil-based lubricant systems, Surf. Topogr. Metrol. Prop. 10 (4) (2022) 045025.
[59] L.X. Zhang, D. Teng, Y.H. Wu, L.Y. Wang, D.P. Song, Mechanism of graphene lubricating oil cooling effect on Si3N4-GCr15 friction pair, Heat Mass Tran. 56 (7) (2020) 2273–2283.
[60] D. Bian, T.V. Aradhyula, Y. Guo, Y. Zhao, Improving tribological performance of chemically bonded phosphate ceramic coatings reinforced by graphene nano-platelets, Ceram. Int. 43 (15) (2017) 12466–12471.
[61] X. Feng, S. Kwon, J.Y. Park, M. Salmeron, Superlubric sliding of graphene nanoflakes on graphene, ACS Nano 7 (2) (2013) 1718–1724.
[62] Y. Guo, W. Guo, C. Chen, Modifying atomic-scale friction between two graphene sheets: a molecular-force-field study, Phys. Rev. B 76 (15) (2007) 155429.
[63] W. Li, L.C. Zhang, C.H. Wu, Z.X. Cui, C. Niu, Y. Wang, Debris effect on the surface wear and damage evolution of counterpart materials subjected to contact sliding, Advances in Manufacturing (2022) 1–15.
[64] M. Belmonte, C. Ramirez, J. Gonzalez-Julian, J. Schneider, P. Miranzo, M.I. Osendi, The beneficial effect of graphene nanofillers on the tribological performance of ceramics, Carbon 61 (2013) 431–435.
[65] P. Miranzo, M. Belmonte, M.I. Osendi, From bulk to cellular structures: a review on ceramic/graphene composites, J. Eur. Ceram. Soc. 37 (2017) 3649–3672.
[66] A. Nieto, A. Bisht, D. Lahiri, C. Zhang, A. Agarwal, Graphene reinforced metal and ceramic matrix composites: a review, Int. Mater. Rev. 62 (2017) 241–302.
[67] A.K. Kasar, P.L. Menezes, Synthesis and recent advances in tribological appli, J. Adv. Manuf. Technol. 97 (2018) 3999–4019.
[68] A.S. Jbara, Z. Othaman, M.A. Saeed, Structural, morphological and optical investigations of θ-Al_2O_3 ultrafine powder, J. Alloys Compd. 718 (2017) 1–6.